# Characterization, Modeling, and Control of Ni-Ti Shape Memory Alloy based on Electrical Resistance Feedback

Brian Lynch*, Xin-Xiang Jiang†, Alex Ellery‡, Fred Nitzsche§

October 28, 2014

## Abstract

The use of shape memory alloy (SMA) actuators has steadily increased within the fields of aerospace, robotics, and biomedical engineering due to their superior properties compared to other actuation systems. Position control of SMA actuators is difficult due to the highly non-linear behaviour but has been well studied using numerous approaches. Electrical resistance can be used to estimate strain in SMA actuator wire due to a strong correlation between the two parameters. Models that approximate this correlation have so far been limited to single applied load conditions, ignored hysteresis effects, apply only to the specific actuator used during testing, or subject to a combination of these drawbacks. This paper presents a stress-strain-resistance model that accounts for varying applied load, major and minor hysteresis effects, and is normalized in terms of actuator geometry. Results of simulation and a simple position control experiment are demonstrated, validating the performance of the model. Furthermore, a correlation between the model and an augmented version of the Liang & Rogers model is also presented.

*Robert M. Buchan Department of Mining, Queen's University

†Transportation Safety Board of Canada

‡Department of Mechanical & Aerospace Engineering, Carleton University

§Department of Mechanical & Aerospace Engineering, Carleton University

## 1 Introduction

Shape memory alloy is a low-cost, light-weight, and easily integrated alternative to conventional actuators that use hydraulics, electric motors or solenoids [1]. Although the shape memory effect was first discovered in 1932 by Arne Ölander [2], it was subsequently found to be present in a near equiatomic Ni-Ti alloy by researchers at the Naval Ordnance Laboratory – where it was appropriately named *Nitinol* [3]. The superior properties of Nitinol made it attractive from an engineering application perspective, and studies of its thermomechanical properties were then pursued. Since its first successful application as a coupling ring in the F-14 Tomcat [4], Nitinol has been the focus of much research and resulted in numerous applications within such fields as aerospace, biomechanical, and robotics engineering [5] [6] [7].

Despite the fact that Nitinol is difficult to machine and process, its high strength, large actuation stroke, and durability make it a desirable choice for use as an actuator [8]. Furthermore, Nitinol has excellent fatigue properties and is also bio-compatible (making it ideal for in-vivo biomedical applications [9] [10] [11]). The material is typically used in wire form, which results in a number of benefits. It may be modeled as a one-dimensional problem; cooling is maximized due to the high ratio of surface area to volume; and integration within a mechanical system is easily accomplished [12] [13].

The thermomechanical phenomenon that makes shape memory alloy unique is known as the *shape memory effect*. This phenomenon is driven by transformations in the crystal microstructure of shape

memory alloy that depend upon the material's temperature and applied mechanical stress, as well as its exact composition and manufacturing process. At lower temperatures, the material is composed primarily of martensite, while at higher temperatures, the material is composed primarly of austenite [14]. The application of mechanical stress may also consequently result in the formation of martensite even at higher temperatures where austenite is predominant. Transformation between martensite and austenite causes *twinning* and *de-twinning* of the crystal structure elements, a process that allows apparent plastic deformation to be recovered through the application of heat or reduction in applied stress. This is unlike conventional metals that undergo permanent and irreversible plastic deformation due to the propagation of dislocations through slip.

A third phase has also been observed in Nitinol named R-phase (referring to the rhombohedral configuration of the phase's crystal structure). This phase precipitates intermediately during transformations between austenite and martensite. The presence of R-phase is dependent upon similar factors that define the other two phases, such as manufacturing processes, applied heat treatments, and alloy composition. Significant hysteresis behaviour observed in the stress, strain, temperature, and resistivity response of Nitinol is primarily due to the occurrence of R-phase.

Position control of Nitinol actuators is a challenging task that continues to be the focus of much research. Many early actuators were open-loop systems that most often used on-off control. This type of control is sufficient for mechanisms that have two states, such as a valve with only open and closed positions. However, most applications require closed-loop control to handle unpredictable perturbations due to variable ambient conditions and external forces.

Proportional-integral-derivative (PID) control has been used extensively for position control of Nitinol actuations, alone or as part of a larger algorithm. For example, Madill and Wang investigated PI control and demonstrated stability based on L2 criteria [15]. Linear optimal and robust control laws have also been applied successfuly. Lee and Marvoidis implemented a linear-quadratic control law and extended Kalman filter based on the H2 algorithm [16]. Jayender also used a linear-quadratic controller based on the H$\infty$ algorithm and optimized using gain scheduling [17].

Hysteresis effects have been successfully compensated using many types of model-based control laws. Although linear models have been used to improve the response of feedback control laws [18] [19], nonlinear models more accurately capture the actuator behaviour. The commonly used Liang & Rogers model has been applied within a backstepping feedback control law [20] and variable structure control [21]. The similar Brinson model has also been applied in combination with a PID control law [22]. Hysteresis effects have also been compensated through predictive control using a Duhem differential model [23] as well as forward and inverse fuzzy Preisach models [24]. Other techniques that have been studied include sliding mode control [25], time-delay compensation [26], and neural networks [27].

The aforementioned control algorithms all depend upon position feedback using sensors such as encoders, strain gauges, and load cells. Integrating a position sensor into the actuation system results in a significant increase in mass, volume, and complexity (features otherwise considered favourable for shape memory alloy actuators). Although predictive modelling has been used to provide feed-forward control, it is difficult to achieve high precision without position feedback control.

Fortunately, Nitinol exhibits a strong and repeatable correlation between actuator strain and electrical resistance. This correlation is primarily due to the well known relationship between length, $L$, cross-sectional area, $A$, resistivity, $\rho$, and resistance, $R$, shown in equation 1. Resistivity itself also changes according to temperature as shown in equation 2.

$$R = \frac{\rho L}{A} \tag{1}$$

$$\rho = \rho_0 \Big( 1 + \alpha \left( T - T_0 \right) \Big) \tag{2}$$

This relationship may then be applied to each phase of the material and combined using a simple linear mixture rule as shown in equation 3, where $\xi_M$ and $\xi_R$ are the fractions of martensite and R-phase

respectively and $\rho_A$, $\rho_M$, and $\rho_R$ are the resistivities of each phase.

$$\rho = \rho_A (1 - \xi_M - \xi_R) + \rho_M \xi_M + \rho_R \xi_R \qquad (3)$$

Furthermore, applied stress has an indirect impact due to the resulting strain and changes in phase transformation temperatures. The combination of these various dependencies results in a relationship between strain and electrical resistance that is overall non-linear and subject to hysteresis. The width of the hysteresis is also notably larger if R-phase is present in the alloy.

The correlation between strain and electrical resistance can be exploited to give Nitinol actuators a *self-sensing* ability. Passive elements have been used to track structural deformations due to earthquakes [28], and have also been embedded in composite structures for strain monitoring [29]. A linear relationship can be assumed for passive strain monitoring since the alloy remains in a single phase. The strain-resistance correlation has also been integrated into the Liang & Rogers model [30] and Brinson model [31].

Electrical resistance feedback has been successfully applied for position control of Nitinol actuators using many different approaches. Simple methods have been studied where a reference resistance value is used as an indicator of complete actuation, preventing overheating and unnecessary overextension [32], or to enable pre-heating for faster response [33]. Linear models have been used extensively, but are limited to a single applied load or stiffness and rely on the absence of hysteresis effects. Ikuta designed an endoscope employing antagonistic Nitinol actuators controlled by a PID law with resistance feedback and a linear strain-resistance model [34]. Neugebauer also used a linear strain-resistance model but within an energy-based thermomechanical model that formed the basis for feedback linearization control of an actuator [35]. The use of polynomial functions can improve the accuracy of strain-resistance models, but is most often restricted to conditions that minimize hysteresis effects. Arai modelled the strain-resistance correlation using a fourth-order polynomial and controlled an actuator using a PID law based on the model and resistance feedback [36]. Similar approaches were also used by Shi [37] and Zhang and Lin [38].

The effects of hysteresis in the strain-resistance behaviour have been overcome using numerous approaches. Meier switched between separate linear functions for the strain-resistance correlation during heating and cooling [39]. Position control was then achieved using a PID law based on the resistance feedback model. Liu applied fourth-order polynomials within a Duhem differental model for predicting actuator strain, again controlled with a PID law [40]. Artificial neural networks have also been investigated for modelling the hysteresis behaviour. Ma used a neural network to model the major hysteresis response and provide position estimation for a PD control law [41]. Both major and minor hysteresis effects were captured using a neural network model developed by Asua and applied within PID control [42].

These algorithms are able to achieve position control of Nitinol actuators based on resistance feedback. However, many do not account for one or more important considerations: variable applied load, hysteresis behaviour, and generalization for actuator size. In most cases, the strain-resistance correlation is modelled for a fixed applied load or stiffness. Although models developed by Urata [43] as well as Zhang and Lin [38] accounted for variable applied stress, there was no consideration for hysteresis effects in either study. Furthermore, many models are not generalized for Nitinol wire of any length and diameter. Normalization is sometimes performed but without consideration of variable applied load.

This paper presents a model of the stress-strain-resistance behaviour of Nitinol shape memory alloy that accounts for variable applied load, major and minor hysteresis effects, and is normalized in terms of actuator geometry. There are three primary sections: characterization of the actuator response in terms of strain-resistance curves, modelling the heating, cooling, and hysteresis behaviour, and application of the model for actuator position control. The model itself consists of a family of linear curves for heating and cooling paths whose coefficients are defined by polynomial functions of applied stress. Transition be-

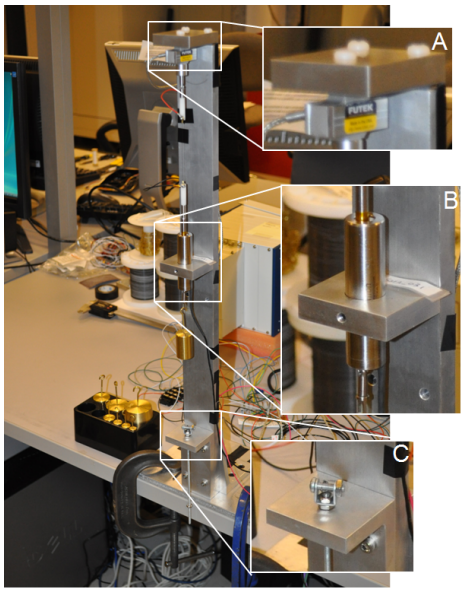


Figure 1: Bench-top experimental setup.

tween the heating and cooling paths is modelled using an exponential function and accounts for major and minor hysteresis. Position control was successfully demonstrated with varying constant applied loads as well as a bias spring load.

## 2 Experimental Setup

Experiments for characterization and control of Nitinol actuatore wire were performed on a bench-top setup shown in figure XXXX. The actuator wire was mounted vertically and hung from a Futek LRF300 load cell attached to the tower. A Solartron Metrology S-Series linear variable displacement transducer (LVDT) was mounted to the tower with the probe attached to the free end of the actuator wire. Constant loading was provided by hanging brass weights from the end of the LVDT probe, while bias spring loading was provided by fixing a spring to the end of the probe (the other end of which was connected to the tower base by a threaded rod). Low-temperature Ni-Ti Flexinol actuator wire was used from Dynalloy.

The electrical resistance of the wire was determined by placing a reference resistor in series and measuring the voltages across the reference and the input terminals. Lead wire resistance was then measured by removing the actuator wire and short-circuiting. Therefore, the actuator wire resistance is given by equation 4, where $R_{SMA}$ is the actuator resistance, $R_{ref}$ is the reference resistance, $V_{net}$ is the total input voltage, $V_{ref}$ is the voltage across the reference resistor, and $R_{lead}$ is the resistance of the lead wires. Note that a small baseline current was required to maintain $V_{ref} > 0$ and avoid division by zero.

$$R_{SMA} = R_{ref}\left(\frac{V_{net}}{V_{ref}} - 1\right) - R_{lead} \qquad (4)$$

Data acquisition was accomplished using a National Instruments system consisting of a PXI-1033 chassis with PXI-6220 and PXI-4110 modules for measurement and power, respectively. The PXI-6220 module was connected to an SCXI-1000 chassis with SCXI-1102 signal conditioner and SCXI-1303 terminal block, through which the sensor outputs are measured. Additionally, the load cell was excited, amplified, and pre-conditioned using an Ectron 563H transducer amplifier/conditioner. The data acquisition system was connected to a Dell Precision 690 computer through a PCIe-8361 card. Measurement and control programs were created and run in LabView 7.1 software.

## 3 Characterization

In order to develop a model for use in position control algorithms, it was important to first characterize the response of the Nitinol actuator wire in terms of stress, strain, and electrical resistance. Experiments were therefore performed to identify the trends in the stress-strain-resistance relationships. The major hysteresis strain-resistance curves were observed during complete actuation and return for a series of varying constant applied loads. Minor hysteresis curves were also observed during incomplete actuation and return. Characterization experiments used open-loop or simple on-off feedback control where the control input was desired electrical current.

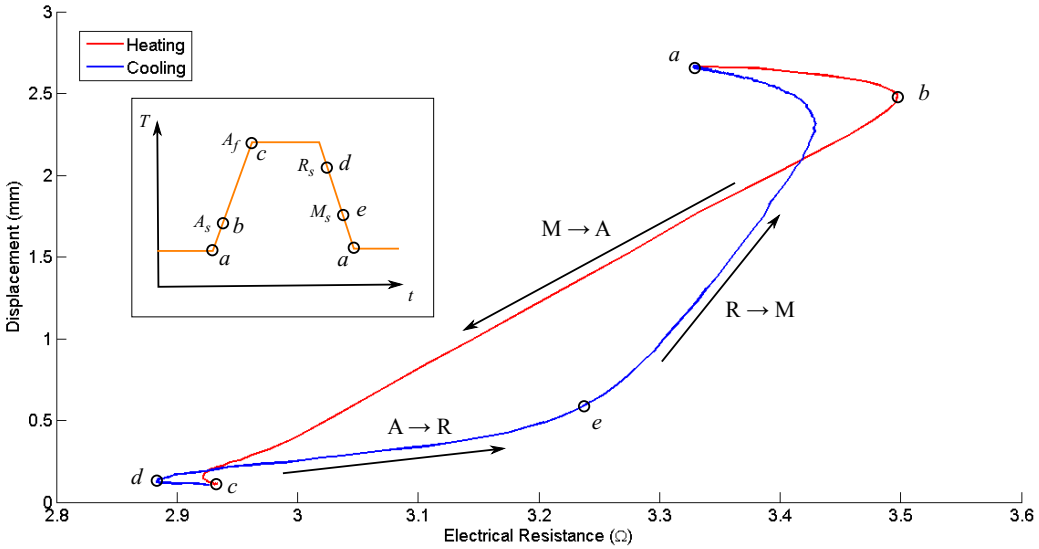


Figure 2: Major hysteresis loop behaviour in the heating and cooling resistance-displacement curves. The inset shows an approximation of the wire temperature during the experiment.

### 3.1 Resistance-Displacement Curves

The complete major hysteresis curve was examined by performing a simple open loop experiment. A constant applied load of approximately 1 N was applied and actuation was achieved using a square wave pulse of current. Figure 2 shows the resulting heating and cooling resistance-displacement curves that form the major hysteresis loop.

The wire starts at a temperature near the martensite finish phase transformation temperature, $M_f$, at point (a). As heating occurs, the temperature reaches the austenite start temperature, $A_s$, at point (b) and phase transformation from martensite to austenite begins. Transformation completes at point (c) where the actuator the austenite finish temperature, $A_f$, at point (c), at which point the actuator is fully contracted. Input current is then removed and the actuator wire cools until reaching the R-phase start temperature, $R_s$, where phase transformation from austenite to R-phase begins. Regardless of complete or incomplete transformation to R-phase, phase transformation to martensite occurs once the actuator reaches the martensite start temperature, $M_s$. The actuator then cools back to the initial temperature while transforming back to martensite.

The response is highly non-linear and results in a large hysteresis effect. However, the resistance-displacement curves can easily be understood considering the relationships defined earlier by equations 1, 2, and 3. Figure 3 shows a simplified approximation of the resistance-displacement hysteresis (using actuation length, $L$, instead of displacement). Lines of constant resistivity are also shown for the phase transformation temperatures. As the actuator heats from point (a) to the start of the martensite-austenite phase transformation at point (b), there is negligible change in length but the increase in temperature causes an increase in resistance. The martensite-austenite phase transformation occurs as temperature increases, but the lower resistivity of austenite results in a decrease in actuator resistance until reaching point (c). Subsequent cooling results in a decrease in resistance until reaching point (d), where

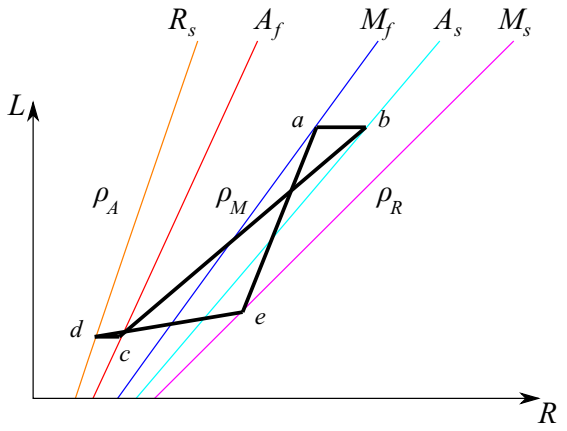


Figure 3: Simplified resistance-displacement response including lines of constant resistivity for martensite at $M_f$, martensite at $A_s$, austenite at $A_f$, austenite at $R_s$, and R-phase at $M_s$.

the austenite-R-phase transformation begins. Due to the much larger resistivity of R-phase, the transformation causes an increase in resistance despite the decrease in temperature. Phase transformation from austenite to R-phase also accounts for some strain recovery as the actuator reaches point (e). Finally, the transformation from R-phase to martensite causes a decrease in resistivity both due to cooling and phase change, but an increase in resistance due to the increase in actuator length.

## 3.2 Influence of Applied Stress

The resistance-displacement behaviour was then characterized for a series of constant applied loads resulting in stress ranging from approximately 15 MPa to 175 MPa. The procedure described in the previous section was used to generate complete actuation responses for each load case. The resulting family of curves are shown in figure 5.

As applied stress increases, there is an expected increase in displacement and resistance at both limits of actuation due to increased elastic strain. The width of the hysteresis also decreases with increasing applied stress. This is due to the change in phase transformation temperatures which causes transformation to martensite to occur sooner during cooling, reducing the amount of R-phase that appears beforehand. Figure 4 demonstrates this relationship between the phase transformation temperatures and applied stress, where it can be seen that $M_s$ becomes greater than $R_s$ at high stress.

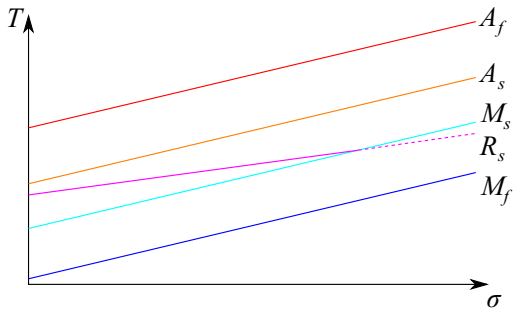


Figure 4: Effect of applied stress on phase transformation temperatures.

## 3.3 Incomplete Actuation

Another important consideration for the model is incomplete actuation, which causes minor hysteresis loops within the resistance-displacement response. Instead of using the open-loop control method previously described, the actuator was commanded to reach a series of test points using on-off feedback control.

Two series of test points were used, incomplete heating and incomplete cooling. During incomplete cooling, the wire is heated to full actuation and then cooled until reaching a desired intermediary position. The wire is subsequently heated and then cooled to the next test point. Incomplete heating is performed similarly, where the wire is partially heated until reaching the test point and then cooled fully. The resulting sets of minor hysteresis loops are shown in figure 6, where a constant load of approximately 1.3 N was applied.

It can be seen that minor hysteresis loops are composed of curves that extend from the point of incomplete actuation and asymptotically approach the

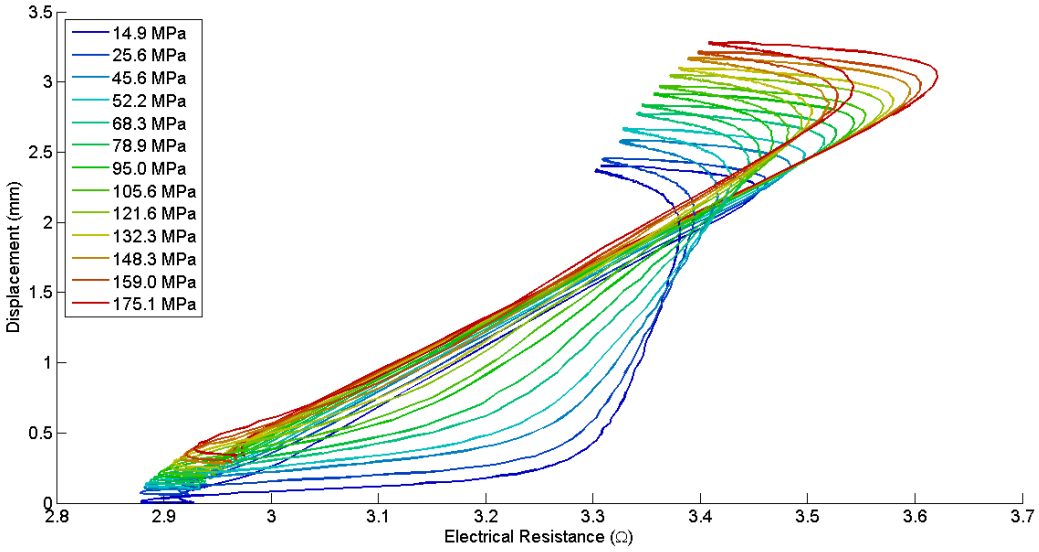


Figure 5: Resistance-displacement curves for a series of constant applied loads.

overall heating or cooling paths. Similar to the major hysteresis behaviour, the minor hysteresis loops occur due to differences in the transformation temperatures as well as the presence of R-phase.

# 4 Modeling

The relationships between stress, strain, and resistance were modelled for the purpose of position control based on resistance feedback as well as feedback of the applied load (either using a load cell or based on known conditions). The model was developed based on the behaviour observed during characterization and captured the three important features: overall heating and cooling paths, minor hysteresis loops, and the influence of applied stress. Linear functions were assumed for the heating and cooling paths, the coefficients of which were modelled as polynomial functions of applied stress. Transition paths during incomplete actuation were modelled using an exponential function for the path slope. The model parameters were then normalized in terms of actuator length and diameter. Correlations between the model and an augmented version of the Liang & Rogers model were also investigated.

## 4.1 Heating & Cooling Curves

The majority of the overall heating and cooling paths are linear, with a highly non-linear and non-deterministic regions at the start and end of transformation. The non-linear regions are ignored and linear functions assumed for modelling the heating and cooling paths separately. Equations 5 and 6 define the heating and cooling paths respectively, where $\delta$ is the displacement and $a$ and $b$ are the linear coefficients (the subscripts $H$ and $C$ denote heating and cooling).

$$\delta_H = a_H R + b_H \tag{5}$$

$$\delta_C = a_C R + b_C \tag{6}$$

Figure 7 shows the linear functions used to approximate heating and cooling paths for the resistance-displacement behaviour observed with an applied

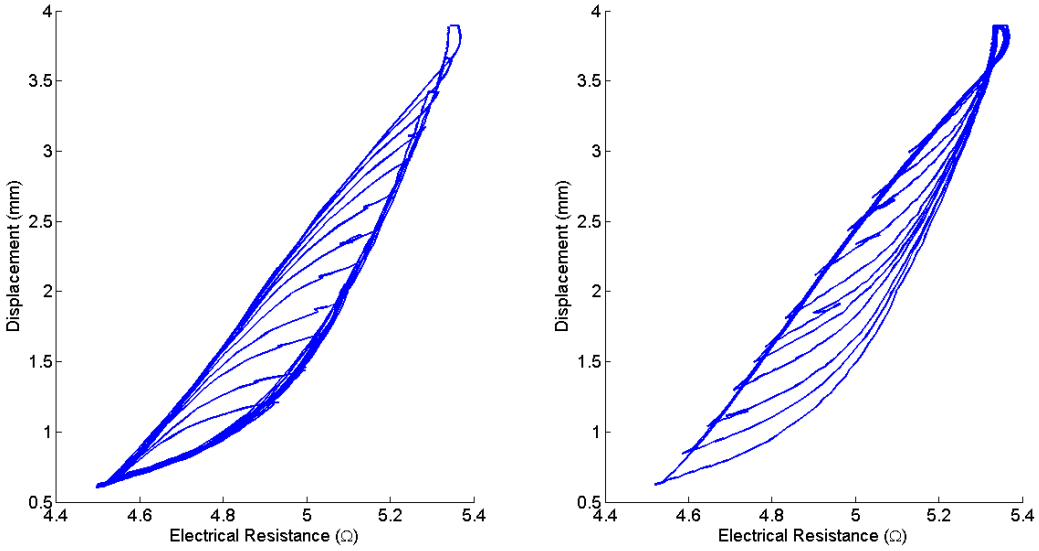


Figure 6: Minor hysteresis loops during incomplete cooling (left) and incomplete heating (right).

load of approximately 0.5 N. Although the linear functions do not capture the behaviour at the limits of actuation, there is a good correlation otherwise.

## 4.2 Influence of Applied Stress

The process of fitting linear functions to the heating and cooling curves of the resistance-displacement response was then repeated for each constant applied load case. The resulting families of linear functions are described in figure 8, where the slope and offset of the heating and cooling curves are plotted as a function of applied stress.

The slope and offset coefficients for cooling change drastically in comparison with those for heating, but all four parameters exhibited non-linear relationships with respect to applied stress. Therefore, polynomial functions were selected for approximating these relationships. Equations 7 to 10 define the slope, $a$, and offset, $b$, for heating and cooling (denoted by subscripts $H$ and $C$), where $\sigma$ is the applied stress, $\beta$ are the polynomial coefficients, and $N$ is the polynomial order.

$$a_H = \sum_{i=0}^{N} \beta_{aH,i} \sigma^{i-1} \tag{7}$$

$$b_H = \sum_{i=0}^{N} \beta_{bH,i} \sigma^{i-1} \tag{8}$$

$$a_C = \sum_{i=0}^{N} \beta_{aC,i} \sigma^{i-1} \tag{9}$$

$$b_C = \sum_{i=0}^{N} \beta_{bC,i} \sigma^{i-1} \tag{10}$$

These coefficients are determined by fitting the polynomial functions to the slope and offset values obtained from experimental data. The resulting approximations are also shown in figure 8 using a polynomial order of 4. While there is a better correlation for the heating coefficients, the overall approach results in a good approximation of the stress influence.

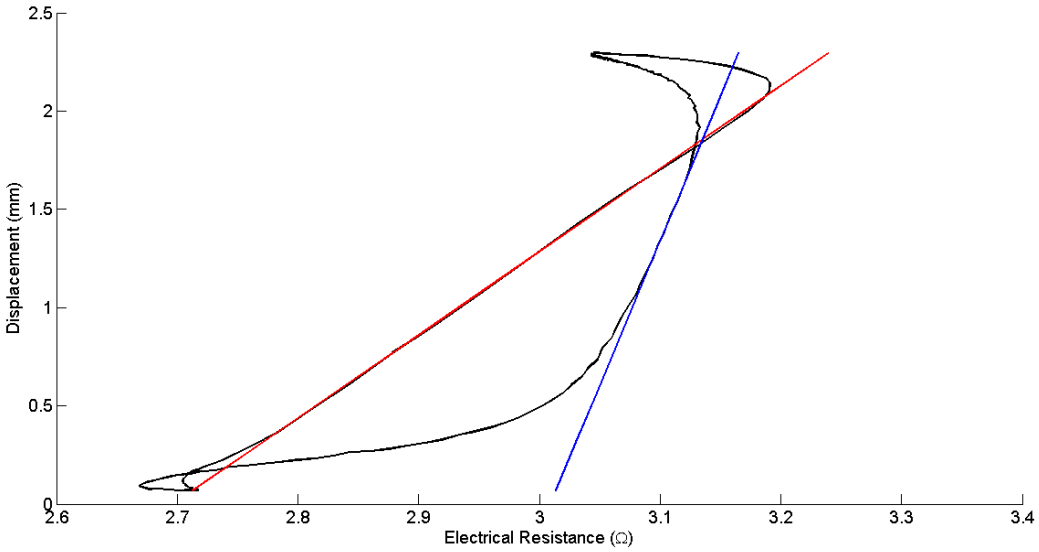


Figure 7: Linear functions for approximating heating and cooling.

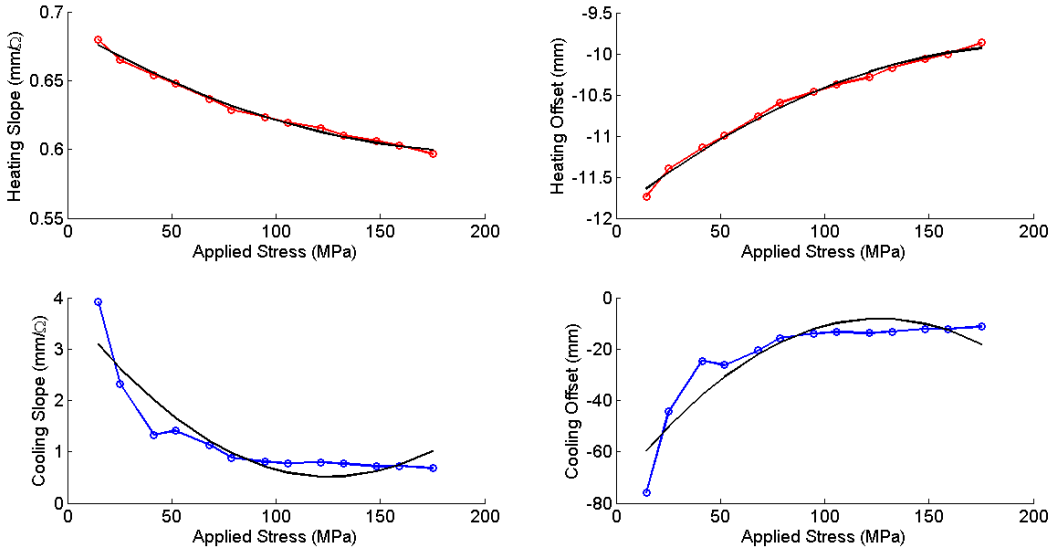


Figure 8: Slope and offset coefficients for heating and cooling curves as a function of applied stress.

### 4.3 Incomplete Actuation

Characterization of the actuator response during incomplete heating and cooling showed that the resistance-displacement curve tended to asymptotically approach the relevant complete heating or cooling curve. This behaviour is modelled using a differential approach, where the slope of the resistance-displacement transition curve, $a$, is determined and the displacement integrated with respect to the change in resistance. The slope starts at a relatively low value and increases continuously until reaching the slope of the relevant heating or cooling curve. An exponential function is used to model the slope of the resistance-displacement curve, where the independent variable is the difference between the current resistance and the expected resistance on the relevant curve at the current displacement.

Equations 11 and 12 define the transition curve during heating, while equations 13 and 14 define the transition curve during cooling. The initial slope, $a_0$, and decay coefficient, $\tau$, are assumed to be constant and determined from analysis of experimental data.

$$a = (a_H - a_0)e^{-\tau z_H} + a_0 \tag{11}$$

$$z_H = R - \frac{\delta - b_H}{a_H} \tag{12}$$

$$a = (a_C - a_0)e^{-\tau z_C} + a_0 \tag{13}$$

$$z_C = \frac{\delta - b_C}{a_C} - R \tag{14}$$

Actuator displacement is then estimated by integration of the slope in the resistance domain, as defined by equation 15, where $R_o$ and $\delta_o$ are the resistance and displacement at the onset of heating or cooling.

$$\delta = \int_{R_o}^{R} a \, \mathrm{d}R + \delta_o \tag{15}$$

In practice, the displacement is estimated using numerical integration according to equation 16, where $k$ is the time index and the slope, $a_k$, is computed based on $R_k$ and $\delta_{k-1}$.

$$\delta_k = a_k \left(R_k - R_{k-1}\right) + \delta_{k-1} \tag{16}$$

The transition model for incomplete actuation is then applied to estimate displacement from experimental characterization data. Figure 9 shows the resulting comparison between experimental data and the model, with both major and minor hysteresis loops captured.

### 4.4 Normalization

The model parameters described so far are determined in terms of electrical resistance, applied stress, and displacement. A calibrated set of model parameters is therefore only applicable to wire of the same length and diameter as that used for characterization. Instead, the model may be normalized with respect to the actuator geometry so that model parameters may be calibrated for a given alloy and applied to actuators of any size.

Normalization of the model was performed by analyzing the response characteristics of actuator wires of various lengths. Figure 10 shows the resulting set of major hysteresis loops for the resistance-displacement response (shown in terms of actuator length instead of displacement). The sets of hysteresis loops appear to grow linearly in terms minimum and maximum resistance and displacement. This is expected since the generalized behaviour is given in terms of resistivity and strain, which are linearly proportional to resistance and displacement respectively.

Resistance is normalized by dividing by the nominal resistance at the purely martensitic state. This nominal martensite resistance is then described in terms of the nominal martensite resistivity and actuator geometry. Equation 17 defines the normalized resistance, $\lambda$, and equation 18 defines the nominal martensite resistance, $R_0$, where $\rho_M$ is the nominal martensite resistivity, $L_0$ is the nominal actuator length, and $A_0$ is the nominal actuator cross-sectional area.

$$\lambda = \frac{R}{R_0} \tag{17}$$

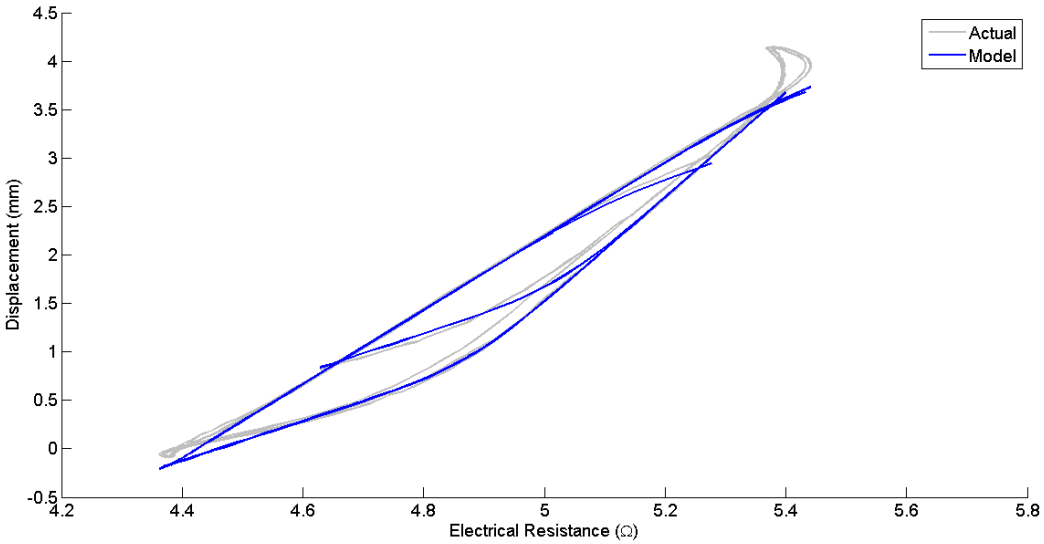


Figure 9: Comparison of transition model and experimental data.

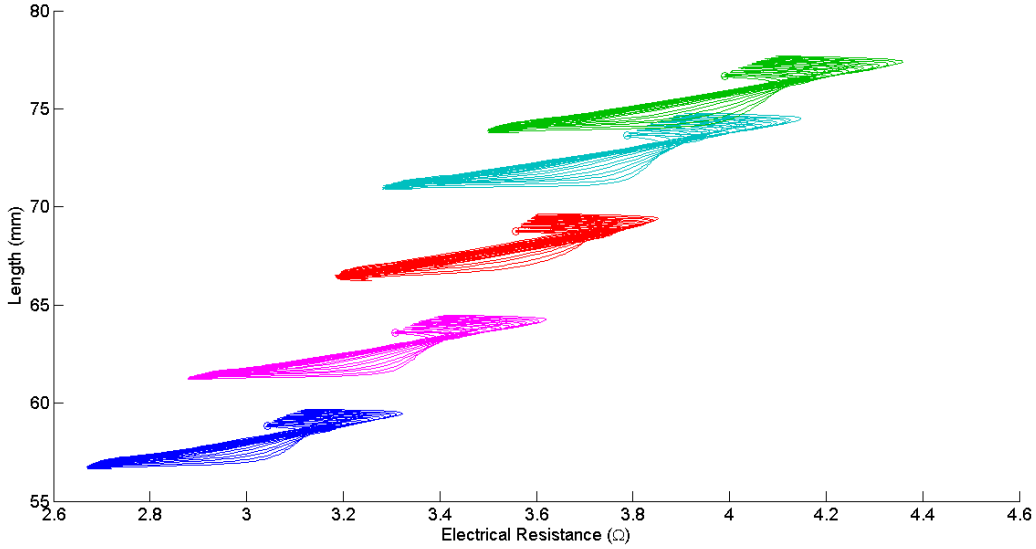


Figure 10: Sets of resistance-displacement response curves for actuator wires of various lengths.

$$R_0 = \frac{\rho_M L_0}{A_0} \tag{18}$$

Actuator displacement is normalized simply by dividing by length, resulting in the actuator strain. Equation 19 defines the actuator strain, $\varepsilon$.

$$\varepsilon = \frac{\delta}{L_0} \tag{19}$$

Normalization was then applied to the resistance-displacement curves shown in figure 10 and the results overlaid for comparison in figure 11. It can be seen that the same hysteresis loops are followed by each actuator in terms of normalized resistance and strain.

The model can therefore be prescribed in terms of normalized parameters for the heating and cooling coefficients, $\tilde{\beta}$, and transition curve coefficients, $\tilde{a}_0$ and $\tilde{\tau}$. These coefficients may be determined from a given sample of actuator wire, as well as the nominal martensite resistivity, $\rho_M$.

Equations 20 and 21 describe the normalized heating and cooling curves, respectively.

$$\varepsilon_H = \tilde{a}_H \lambda + \tilde{b}_H \tag{20}$$

$$\varepsilon_C = \tilde{a}_C \lambda + \tilde{b}_C \tag{21}$$

The normalized slope and offset coefficients are then defined by equations 22 to 25.

$$\tilde{a}_H = \sum_{i=0}^{N} \tilde{\beta}_{aH,i} \sigma^{i-1} \tag{22}$$

$$\tilde{b}_H = \sum_{i=0}^{N} \tilde{\beta}_{bH,i} \sigma^{i-1} \tag{23}$$

$$\tilde{a}_C = \sum_{i=0}^{N} \tilde{\beta}_{aC,i} \sigma^{i-1} \tag{24}$$

$$\tilde{b}_C = \sum_{i=0}^{N} \tilde{\beta}_{bC,i} \sigma^{i-1} \tag{25}$$

The slope of the normalized transition curves during heating and cooling are then defined by equations 26 and 27, respectively.

$$\tilde{a} = (\tilde{a}_H - \tilde{a}_0) e^{-\tilde{\tau}\left(\lambda - \frac{1}{\tilde{a}_H}\left(\varepsilon - \tilde{b}_H\right)\right)} + \tilde{a}_0 \tag{26}$$

$$\tilde{a} = (\tilde{a}_C - \tilde{a}_0) e^{-\tilde{\tau}\left(\frac{1}{\tilde{a}_C}\left(\varepsilon - \tilde{b}_C\right) - \lambda\right)} + \tilde{a}_0 \tag{27}$$

Equation 28 then defines the strain estimated from numerical integration of the slope in the normalized resistance domain.

$$\varepsilon_k = \tilde{a}_k \left(\lambda_k - \lambda_{k-1}\right) + \varepsilon_{k-1} \tag{28}$$

The estimated displacement is then determined based on the nominal actuator length using equation 19.

New actuator wires are modelled by first computing the nominal martensite resistance, $R_0$, which is then used to normalize the measured resistance. Strain is estimated from the model based on normalized resistance, $\lambda$, and applied stress, $\sigma$, and then converted to displacement for position feedback.

## 4.5 Simulation

The performance of the model was validated through simulation after determining the model parameters from experimental characterization data. The purpose of simulation was to verify the suitability of the integrated model when applied to experimental data. Electrical resistance and applied stress measurements were input into the model and the estimated actuator displacement compared to the measured value. Data from simple actuation experiments used during characterization was used that included incomplete heating and cooling segments as well as various constant applied loads and spring constraint loading.

Figures 12 and 13 show simulation results for experiments performed with constant applied loads of 0.49 N and 0.98 N, respectively, while figure 14 shows results using a spring constraint. The model provides a good estimation of the actuator displacement, with the exception of the highly non-linear and indeterminate martensitic region. The overall mean error was approximately 2.1% of the nominal actuator displacement (defined as 4% of the actuator length).

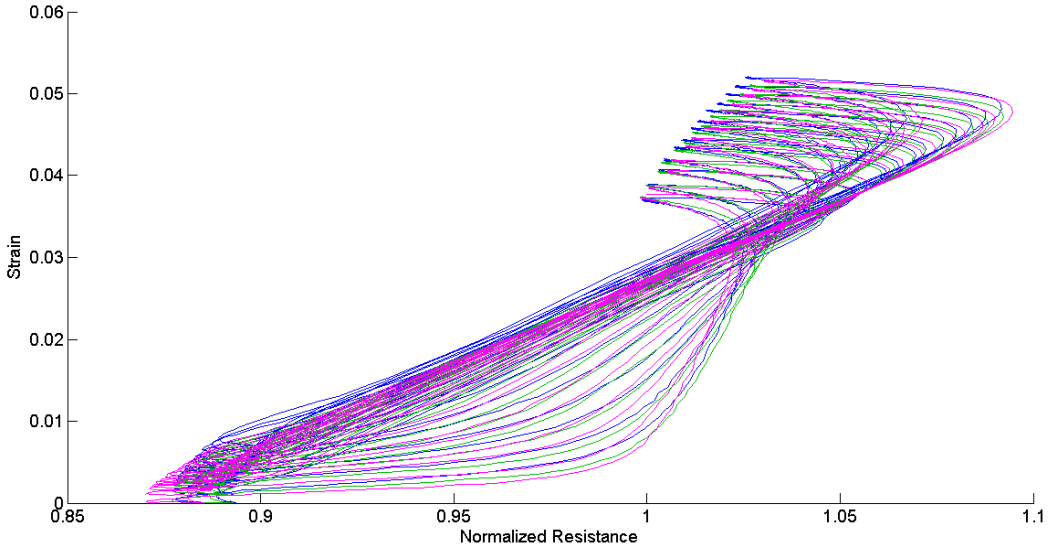


Figure 11: Normalized resistance-displacement curves overlaid for comparison.

The ability of the model to capture the influence of varying applied load is verified by the successfully position estimation under both constant loads, but especially by the results obtained using the spring constraint. Since the applied stress varies with actuator displacement, the linear coefficients for the heating and cooling paths are being modified throughout the hysteresis loop. Although the model was not developed with this consideration in mind, experimental results demonstrate that the method is valid.

The importance of accounting for varying applied load is shown in figure 15, where a constant applied load is incorrectly assumed for an actuator with spring constraint load conditions. There is a significant increase in the model error due to the incorrectly assumed coefficients for the heating and cooling paths, which results in a mean error of approximately 7.8% (almost four times the mean error when varying stress is properly included). This emphasizes the need to include the influence of applied stress within the model.

The resulting resistance-displacement curves for each simulation are shown in figures 16 to 19.

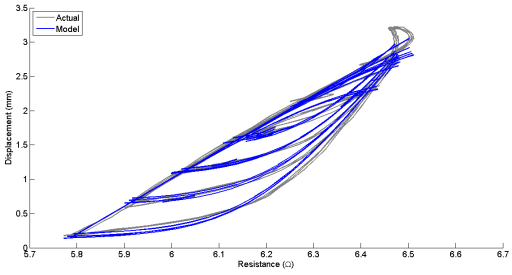


Figure 16: Simulated resistance-displacement curves for a constant applied load of 0.49 N.

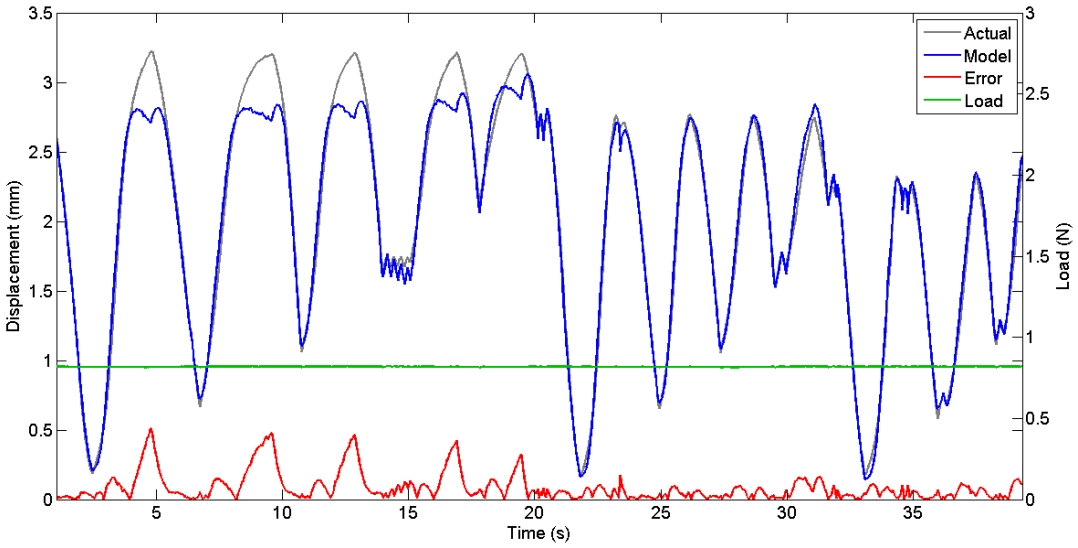


Figure 12: Simulation results under constant applied load of 0.49 N.

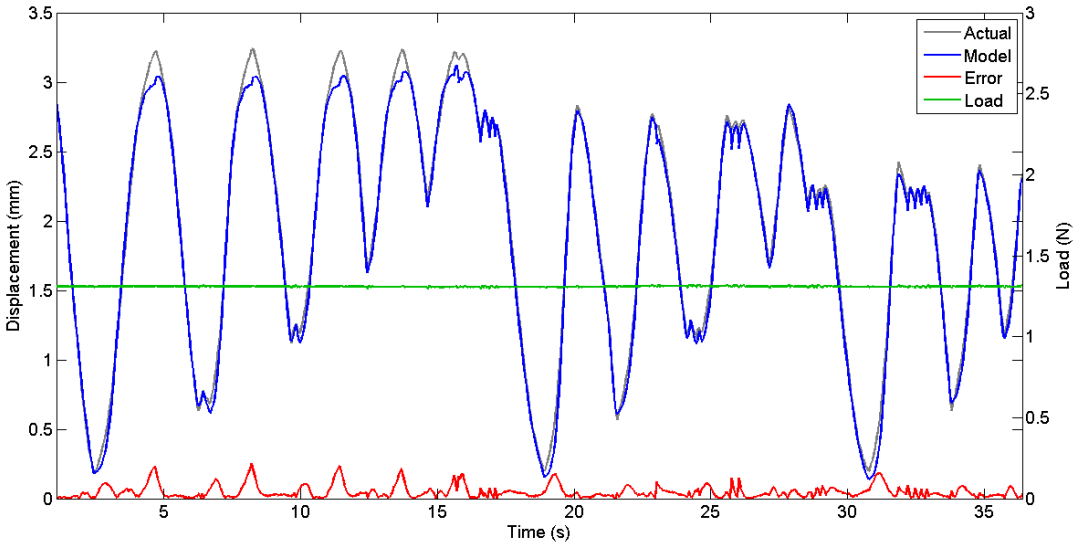


Figure 13: Simulation results under constant applied load of 0.98 N.

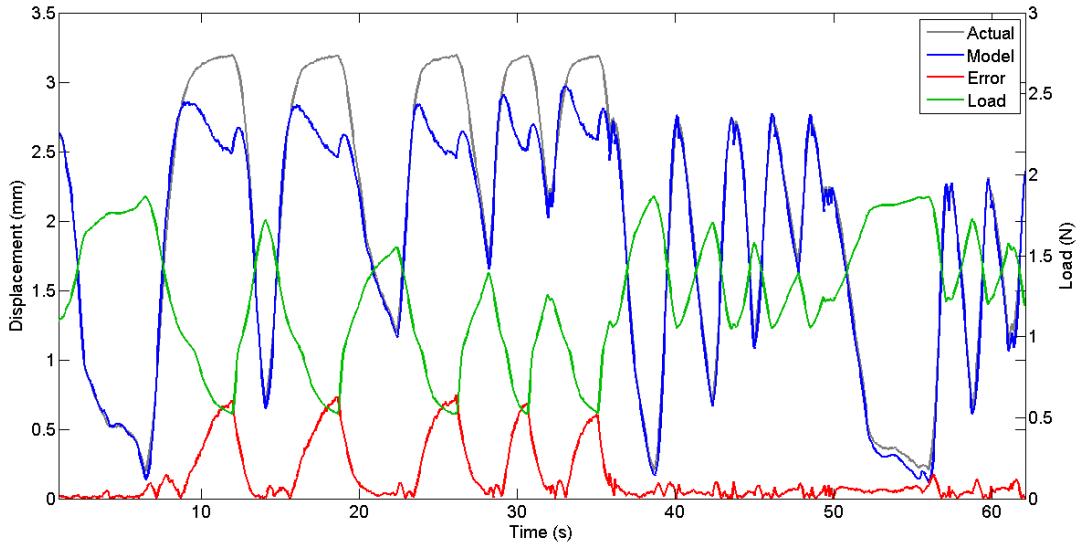


Figure 14: Simulation results under spring constraint loading conditions.

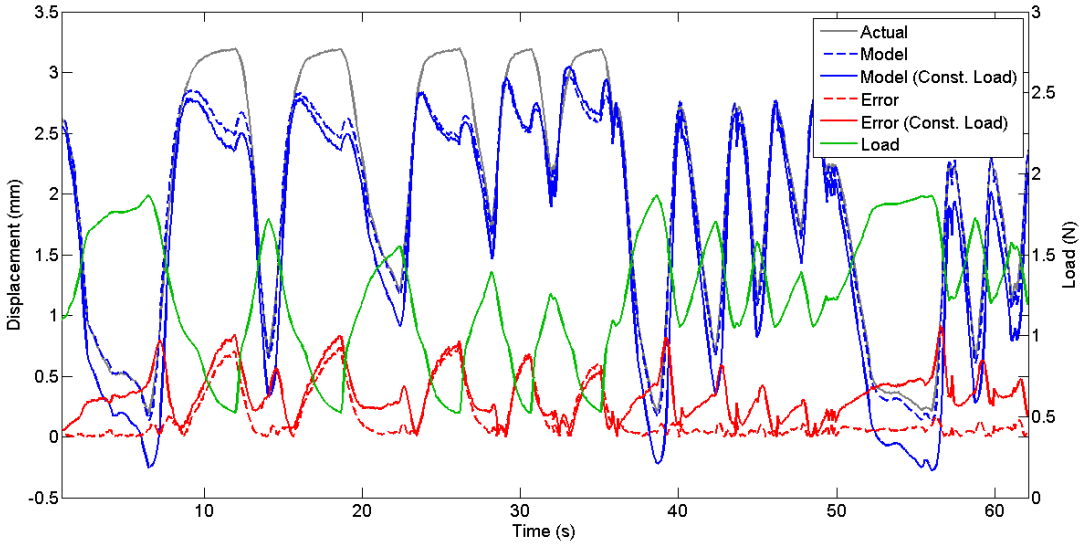


Figure 15: Simulation results under spring constraint loading conditions but with constant applied load assumed.

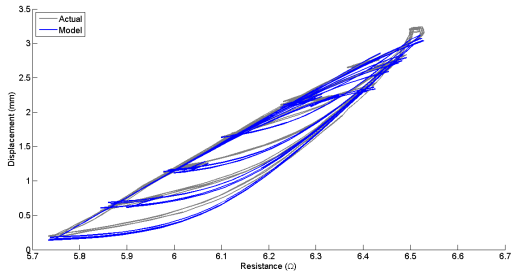


Figure 17: Simulated resistance-displacement curves for a constant applied load of 0.98 N.

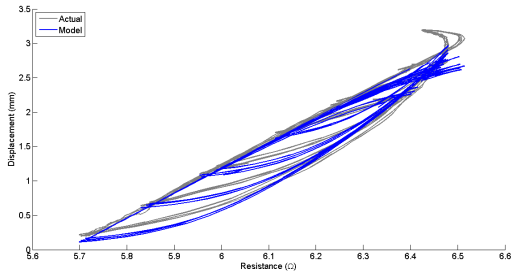


Figure 18: Simulated resistance-displacement curves for the spring constraint loading condition.

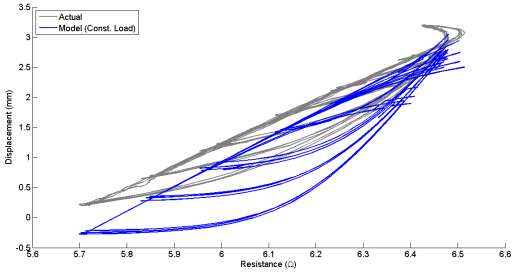


Figure 19: Simulated resistance-displacement curves for the spring constraint loading condition with constant applied load assumed.

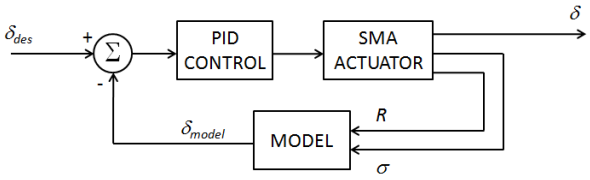


Figure 20: PID control law used for position control using resistance and applied load feedback.

# 5 Position Control

Simulation results showed that the model is capable of estimating the actuator displacement through complete and incomplete actuation as well as under varying load conditions. The performance of the model was then tested within a simple position control application. Electrical resistance and applied load were measured and input to the model. The resulting estimate of actuator displacement was then used as position feedback within a PID control law with wire current as the input, as described by figure 20. Gains were selected by trial and error to achieve stability and a reasonable settling time, resulting in a satisfactory underdamped response. Threshold limits were also applied to the desired wire current value, preventing too much current input as well as maintaining the minimum baseline current.

More elaborate control algorithms or careful selection of PID gains could be used to improve the feedback control response. However, this position control experiment was intended to simply test the performance of the model under expected application conditions. Although the performance of the controller is dictated by the error between desired and actual displacement, the performance of the model is dictated by the error between estimated and actual displacement.

Figure 21 demonstrates the results of applying the model for position control. Varying applied load was achieved using the spring constraint condition. The desired displacement signal consisted of stepping through a series of randomly generated positions and holding at each one for 20 s after settling. The performance of the model is similar to that observed during

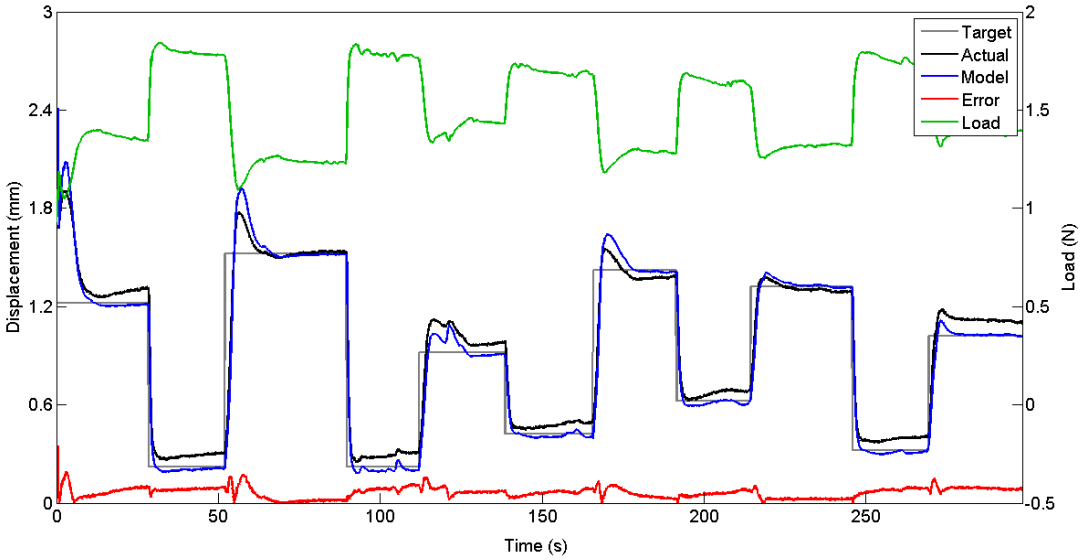


Figure 21: Results of applying the model in a simple position control experiment with varying applied load.

simulation, with a mean error of approximately 2.2%.

# 6 Model Correlations

The model presented in this paper has been developed in terms of actuator stress, strain, and electrical resistance. Temperature is not included as a model variable even though it is the driving parameter behind the phase transformations. Algorithms such as the Liang & Rogers model require both temperature and applied stress as independent variables for estimating strain, and were not considered for use during the development of the model. However, significant correlations were found between the presented model and an augmented version of the Liang & Rogers model studied by Brammajyosula [30]. The augmented model includes the presence of R-phase and was used by Brammajyosula to predict actuator strain and electrical resistance based on temperature and stress inputs.

The Liang & Rogers model consists of a constitutive equation describing the stress-strain relationship (including terms for thermal expansion and transformation strain) and forward and reverse phase transformation equations defining the phase fractions. Equation 29 is the simplified constitutive equation, where $E$ is the Young's modulus, $\varepsilon_L$ is the transformation strain, $\xi_M$ is the fraction of martensite, and thermal expansion has been ignored since it is negligible in comparison with the other terms.

$$\varepsilon = \frac{\sigma}{E} + \varepsilon_L \xi_M \tag{29}$$

The Young's modulus is defined by the simple mixing rule in equation 30, where $E_A$ and $E_M$ are the moduli of austenite and martensite, respectively.

$$E = E_M \xi_M + E_A \left(1 - \xi_M\right) \tag{30}$$

The fraction of martensite is defined by the temperature and stress states. If the temperature is low enough, the material is entirely martensite and $\xi_M = 1$, whereas if the temperature is high enough the material is entirely austenite and $\xi_M = 0$. Phase transformation from martensite to austenite is defined by equation 31 if heating occurs and the temperature and stress states satisfy the inequality in

equation 32.

$$\xi_M = \frac{\xi_{M0}}{2}\left\{\cos\left[\frac{\pi}{A_f - A_s}\left(T - A_s - \frac{\sigma}{C_A}\right)\right] + 1\right\} \tag{31}$$

$$A_s + \frac{\sigma}{C_A} < T < A_f + \frac{\sigma}{C_A} \tag{32}$$

Phase transformation from austenite to martensite is defined by equation 33 if cooling occurs and the temperature and stress states satisfy the inequality in equation 34.

$$\xi_M = \frac{1 - \xi_{M0}}{2}\left\{\cos\left[\frac{\pi}{M_s - M_f}\left(T - M_f - \frac{\sigma}{C_M}\right)\right] + 1\right\} + \xi_{M0} \tag{33}$$

$$M_f + \frac{\sigma}{C_M} < T < M_s + \frac{\sigma}{C_M} \tag{34}$$

Brammajyosula modified this algorithm slightly to include the R-phase fraction, $\xi_R$, adding another phase transformation equation as well as including separate transformation strains for martensite and R-phase. The mixing rules used to determine materials properties were also slightly modified to include R-phase terms.

The resistance-displacement response was then simulated using the Brammajyosula algorithm at various levels of applied stress. Temperature was ramped up from below $M_s$ to above $A_f$ and then ramped back down, resulting in complete forward and reverse transformation. The response is shown in figure 22, where the behaviour observed during experimental characterization is represented.

A comparison was then made between the Brammajyosula model and the model presented in this paper. The linear heating and cooling curves are described by coefficients that are functions of applied stress. These coefficients can also be determined analytically from the Brammajyosula model by defining two points on each of the heating and cooling curves. The heating curve is defined by the limits of the transformation from martensite to austenite, while the cooling curve is defined by the limits of transformation from R-phase to martensite. Expressions for both the displacement and electrical resistance must be determined at each point. Note that electrical resistance is determined using equations 1 to 3 where constant volume is assumed when accounting for strain, resulting in equation 35.

$$R = \frac{\rho L_0}{A_0}(1 + 2\varepsilon) \tag{35}$$

The slope and offset for the linear heating function are determined by equations 36 and 37, respectively.

$$a_H = \frac{\delta_{Hs} - \delta_{Hf}}{R_{Hs} - R_{Hf}} \tag{36}$$

$$b_H = \frac{\delta_{Hf} R_{Hs} - \delta_{Hs} R_{Hf}}{R_{Hs} - R_{Hf}} \tag{37}$$

Equations 38 to 41 define the start and finish resistance and displacement during heating, where the material starts in the martensite phase at $A_s$ and finishes in the austenite phase at $A_f$.

$$R_{Hs} = \frac{\rho_M L_0}{A_0}\left(1 + \alpha_M\left(A_s + \frac{\sigma}{C_A} - T_0\right)\right)\left(1 + 2\left(\varepsilon_{LM} + \frac{\sigma}{E_M}\right)\right) \tag{38}$$

$$R_{Hf} = \frac{\rho_A L_0}{A_0}\left(1 + \alpha_A\left(A_f + \frac{\sigma}{C_A} - T_0\right)\right)\left(1 + 2\frac{\sigma}{E_A}\right) \tag{39}$$

$$\delta_{Hs} = L_0\left(\varepsilon_{LM} + \frac{\sigma}{E_M}\right) \tag{40}$$

$$\delta_{Hf} = L_0 \frac{\sigma}{E_A} \tag{41}$$

The slope and offset during cooling are similarly defined by equations 42 and 43.

$$a_C = \frac{\delta_{Cf} - \delta_{Cs}}{R_{Cf} - R_{Cs}} \tag{42}$$

$$b_C = \frac{\delta_{Cs} R_{Cf} - \delta_{CF} R_{Cs}}{R_{Cf} - R_{Cs}} \tag{43}$$

The resistance and displacement at the start and finish of the cooling phase transformation are defined by equations 44 to 47, where the material starts at a mixture of R-phase and austenite at $M_s$ and finishes in the martensite phase at $M_f$.

$$R_{Cs} = \frac{\rho_{Cs} L_0}{A_0}\left(1 + 2\left(\varepsilon_{LR} + \frac{\sigma}{\xi_R E_R + (1 - \xi_R) E_A}\right)\right) \tag{44}$$

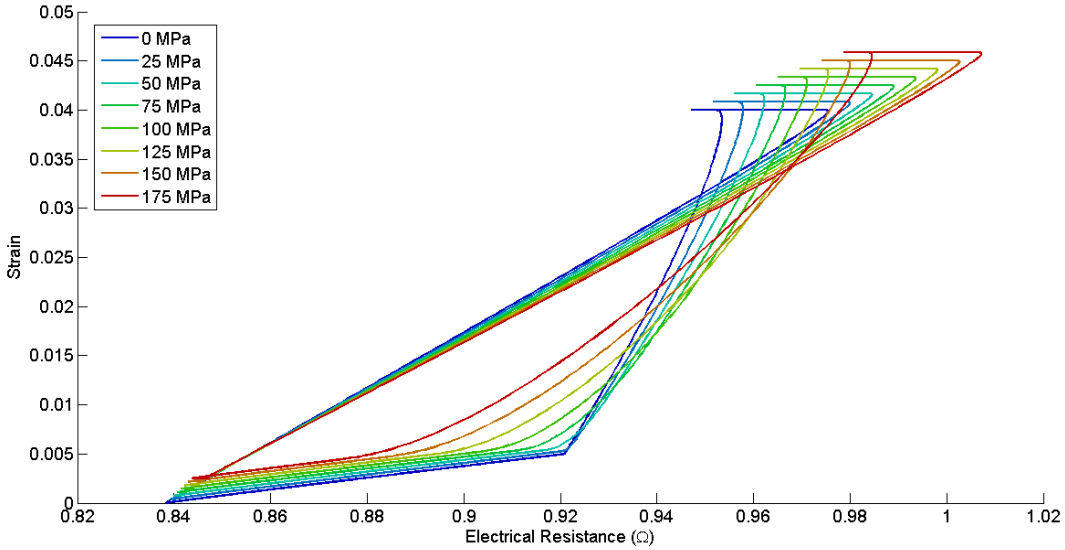


Figure 22: Simulated resistance-displacement curves using the augmented Liang & Rogers model developed by Brammajyosula.

$$R_{Cf}=\frac{\rho_M L_0}{A_0}\left(1+\alpha_M\left(M_f+\frac{\sigma}{C_M}-T_0\right)\right)\left(1+2\left(\varepsilon_{LM}+\frac{\sigma}{E_M}\right)\right) \tag{45}$$

$$\delta_{Cs} = L_0\left(\varepsilon_{LR}+\frac{\sigma}{\xi_R E_R+(1-\xi_R)E_A}\right) \tag{46}$$

$$\delta_{Cf} = L_0\left(\varepsilon_{LM}+\frac{\sigma}{E_M}\right) \tag{47}$$

The fraction of R-phase at the start must be determined as shown in equation 48 and used to determine resistivity as defined by equation 49 as well as the elastic modulus in equations 44 and 46.

$$\xi_R=\frac{1}{2}\left(\cos\left(\frac{\pi}{R_s-R_f}\left(M_s+\frac{\sigma}{C_M}-R_f-\frac{\sigma}{C_R}\right)\right)+1\right) \tag{48}$$

$$\begin{aligned}\rho_{Cs} = {} & \xi_R\rho_R\left(1+\alpha_R\left(M_s+\frac{\sigma}{C_M}-T_0\right)\right) \\ & +(1-\xi_R)\,\rho_A\left(1+\alpha_A\left(M_S+\frac{\sigma}{C_M}-T_0\right)\right)\end{aligned} \tag{49}$$

Substitution of the relevant equations results in relationships for the heating and cooling slope and offset coefficients that are functions of applied stress. These functions were then evaluated at the levels of applied stress used during experimental characterization and modeling. Figure 23 shows the resulting correlation between the coefficients fitted to experimental data, the polynomial functions used to approximate the curves, and the analytically determined values using the Brammajyosula model.

Considering that the material parameters were used for a different Ni-Ti alloy (in the absence of known values for Flexinol), there is a good correlation between the experimentally and analytically determined values. Therefore, it may be possible

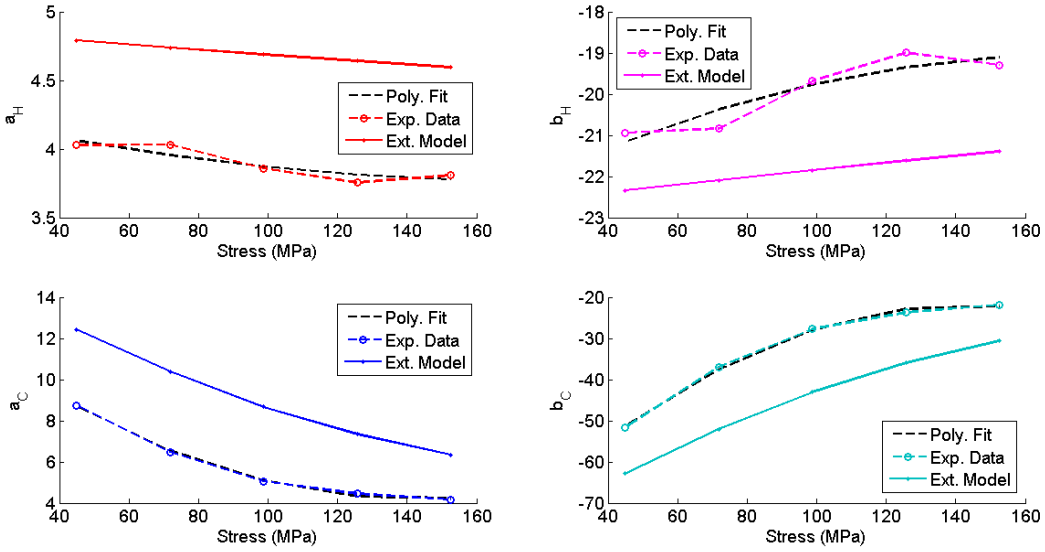


Figure 23: Correlations between experimental data, polynomial fitting functions, and the analytical results.

to define the linear heating and cooling coefficient functions analytically instead of using polynomials after identifying the material properties. Although the transition functions for completing the hysteresis model were not studied analytically, the resulting curves shown in figure 22 suggest that similar correlations may exist.

# 7 Conclusions

The model presented in this paper successfully captured the key features of the stress-strain-resistance behaviour of Nitinol shape memory alloy. Experimental characterization revealed significant hysteresis effects in the resistance-displacement response that varied with the level of applied stress.

Heating and cooling paths were found to be generally linear and therefore modelled as such. The coefficients for the linear heating and cooling paths were themselves defined as polynomial functions of applied stress. Transition between the heating and cooling curves was modelled using an exponential function that captured both major and minor hysteresis effects.

Actuator wires of various lengths were also studied and showed that the response characteristics are linearly proportional to the wire length. This allowed the model to be normalized in terms of the actuator geometry for more generalized application.

The performance of the model was validated through simulation based on recorded experimental data and within a simple position control application. In both cases, the model had a mean error of approximately 2% of the nominal actuator stroke and handled the effect of varying applied load. Although a simple PID control law was used with position feedback provided by the model estimation of actuator displacement, more sophisticated algorithms could be used to improve the controller performance.

The model was also compared to an augmented version of the Liang & Rogers model. The linear heating and cooling coefficients were defined analytically and estimated for a series of applied stress levels using an assumed set of material properties. Good correlations between the resulting curves demon-

strated that the model coefficients may possibly be estimated analytically instead of determined experimentally.

It is expected that this model may be useful for future applications of Nitinol actuator position control based on electrical resistance feedback. The model assumes feedback of the applied stress is also provided, but may possibly be replaced by a known value or model depending on the boundary conditions. Other functions may possibly be used to replace and improve upon the linear and polynomial functions. However, the results of this study demonstrate the feasibility of modelling the stress-strain-resistance behaviour of Nitinol actuator wire considering major and minor hysteresis effects, varying applied load, and normalization in terms of geometry.

# References


[1] Constantinos Mavroidis, Charles Pfeiffer, and Michael Mosley. Conventional actuators, shape memory alloys, and electrorheological fluids. *Invited Chapter in Automation, Miniature Robotics and Sensors for Non-Destructive Testing and Evaluation*, 1999.

[2] Arne Ölander. An electrochemical investigation of solid cadmium-gold alloy. *Journal of the American Chemical Society*, 54(10):3819–3833, 1932.

[3] W.J. Buehler and R.C. Wiley. Report noltr 61-75 (ad 266607). Technical report, U.S. Naval Ordnance Laboratory, 1961.

[4] Ming H. Wu and L. McD. Schetky. Industrial applications for shape memory alloys. *Proceedings of the International Conference on Shape Memory and Superelastic Technolgies*, pages 171–182, 2000.

[5] D.J. Hartl and D.C. Lagoudas. Aerospace applications of shape memory alloys. *Proceedings of the Institution of Mechanical Engineers, Part G: Journal of Aerospace Engineering*, 221:535–553, 2007.

[6] Lorenza Petrini and FrancescoMigliavacca. Biomedical applications of shape memory alloys. *Journal of Metallurgy*, pages 1–15, 2011.

[7] T. Raparelli, P. Beomonte Zobel, and F. Durante. A robot actuated by shape memory alloy wires. *Proceedings of the 2002 IEEE International Symposium on Industrial Electronics*, pages 420–423, 2002.

[8] Muhammad A. Rahman. Patents on superelastic shape memory alloy. *Recent Patents on Mechanical Engineering*, 1:65–67, 2008.

[9] F.X. Gil, J.M. Manero, and J.A. Planell. Relevant aspects in the clinical applications of niti shape memory alloys. *Journal of Materials Science: Materials in Medicine*, 7:403–406, 1996.

[10] D.Tarnita, D. N. Tarnita, Roxana Tarnita, Cosmin Berceanu, and Florin Cismaru. Modular adaptive bone plate connected by nitinol staple. *Materialwissenschaft und Werkstofftechnik*, 41-12:83–93, 2010.

[11] Dominiek Reynaerts, Jan Peirs, and Hendrik Van Brussel. Design of a shape memory alloy actuated implantable drug delivery system. *Eurosensors X*, pages 1185–1188, 1996.

[12] A.D. Johnson, V. Gupta, V. Martynov, and L. Menchaca. Silicon oxide diaphragm valves and pumps with tini thin film actuation. *Proceedings of the International Conference on Shape Memory and Superelastic Technologies 2003*, pages 605–612, 2004.

[13] D. Mandru, I. Lungu, S. Noveanu, and O. Tatar. Shape memory alloy wires as actuators for a minirobot. *2010 IEEE International Conference on Automation, Quality and Testing, Robotics*, pages 4–7, 2010.

[14] Xiangyang Huang, Graeme J. Ackland, and Karin M. Rabe. Crystal structures and shape-memory behaviour of niti. *Nature Materials*, 2:307–311, 2003.

[15] Daniel R. Madill and David Wang. Modeling and l2-stability of a shape memory alloy position control system. *IEEE Transactions on Control Systems Technology*, 6-4:473–481, 1998.

[16] Chunhao Joseph Lee and Constantinos Mavroidis. Analytical dynamic model and experimental robust and optimal control of shape-memory-alloy bundle actuators. *Proceedings of the 2002 ASME International Mechanical Engineering Congress and Exposition*, pages 491–498, 2002.

[17] J. Jayender, R. V. Patel, S. Nikumb, and M. Ostojic. Modeling and control of shape memory alloy actuators. *IEEE Transactions on Control Systems Technology*, 16-2:279–287, 2008.

[18] Kazuhiko Arai, Shinji Ararnaki, and Kazulaisa Yanagisawa. Feedback linearization for sma (shape memory alloy). *Proceedings of the 34th SICE*

*Annual Conference. International Session Papers*, pages 1383–1386, 1995.

[19] H. Benzaoui, N. Chaillet, C. Lexcellent, and A. Bourjault. Non linear motion and force control of shape memory alloys actuators. *Proceedings of the SPIE Conference on Mathematics and Control in Smart Structures*, 3667:337–348, 1999.

[20] M. Elahinia, J. Koo, M. Ahmadian, and C. Woolsey. Backstepping control of a shape memory alloy actuated robotic arm. *Journal of Vibration and Control*, 11:407–429, 2005.

[21] Hashem Ashrafiuon, Mojtaba Eshraghi, and Mohammad H. Elahinia. Position control of a three-link shape memory alloy actuated robot. *Journal Of Intelligent Material Systems and Structures*, 17:381–393, 2006.

[22] Sumiko Majima, Kazuyuki Kodama, and Tadahiro Hasegawa. Modeling of shape memory alloy actuator and tracking control system with the model. *IEEE Transactions on Control Systems Technology*, 9-1:54–59, 2001.

[23] Sushant M. Dutta, Fathi H. Ghorbel, and James B. Dabney. Modeling and control of a shape memory alloy actuator. *Proceedings of the 2005 IEEE International Symposium on Intelligent Control*, pages 1007–1012, 2005.

[24] Kyoung Kwan Ahn and Nguyen Bao Kha. Internal model control for shape memory alloy actuators using fuzzy based preisach model. *Sensors and Actuators A*, 13:730–741, 2006.

[25] G. Song. Robust position regulation of a rotary servo actuated by a shape memory alloy wire. *2001 IEEE International Symposium on Industrial Electronics Proceedings*, 3:1923–1928, 2001.

[26] Hyo Jik Lee and Jung Ju Lee. Time delay control of a shape memory alloy actuator. *Smart Materials and Structures*, 13:227–239, 2004.

[27] G. Song, V. Chaudhry, and C. Batur. A neural network inverse model for a shape memory alloy wire actuator. *Journal Of Intelligent Material Systems and Structures*, 14:371–378, 2003.

[28] C.X. Mao, H. Li, and J.P. Ou. Experimental study on shape memory alloy displacement transducer. *Earth and Space Conference 2008: Proceedings of the 11th Aerospace Division International Conference on Engineering, Science, Construction, and Operations in Challenging Environments*, 323:1–8, 2008.

[29] G. Triantafyllou and G.C. Psarras. Probing the reverse martensitic transformation in constrained shape memory alloys via electrical resistance. *Journal of Intelligent Material Systems and Structures*, 21:975–982, 2010.

[30] Ravindra Brammajyosula, Vidyashankar Buravalla, and Ashish Khandelwal. Model for resistance evolution in shape memory alloys including r-phase. *Smart Materials and Structures*, 20:1–11, 2011.

[31] Di Cui, Gangbing Song, and Hongnan Li. Modeling of the electrical resistance of shape memory alloy wires. *Smart Materials and Structures*, 9-5:1–9, 2010.

[32] Roy Featherstone and Yee Harn Teh. Improving the speed of shape memory alloy actuators by faster electrical heating. *Proceedings of the International Symposium of Experimental Robotics*, pages 18–21, 2004.

[33] M. El Dib, R. Gorbet, E. Kubica, X. Gao, A.L. Browne, and N.L. Johnson. Adaptive sma actuator priming using resistance feedback. *Smart Materials and Struct*, 20:1–14, 2011.

[34] M. Mertmann and E. Hornbogen. Grippers for the micro assembly containing shape memory actuators and sensors. *Journal de Physique IV*, 7-C5:621–626, 1997.

[35] Reimund Neugebauer, Andre Bucht, Kenny Pagel, and Jakob Jung. Numerical simulation of the activation behavior of thermal shape memory alloys. *Proceedings of Industrial and Commercial Applications of Smart Structures Technologies 2010*, 7645:1–12, 2010.

[36] Fumihito Arai, Daisaku Azuma, Keisuke Narumi, Yoko Yamanishi, and Yu-Ching Lin. Design and fabrication of a shape memory alloy actuated exoskeletal microarm. *Proceedings of the 2007 18th International Symposium on Micro-NanoMechatronics and Human Science*, pages 148–152, 2007.

[37] Zhenyun Shi, Da Liu, Cheng Ma, and Depeng Zhao. Accurate controlled shape memory alloy actuator for minimally invasive surgery. *Proceedings of the 2011 IEEE International Conference on Mechatronics and Automation*, pages 817–822, 2011.

[38] Jianjun Zhang and Yuehong Yin. Sma-based bionic integration of self-sensor-actuator for artificial skeletal muscle. *Sensors and Actuators A*, 181:94–102, 2012.

[39] H. Meier, A. Czechowicza, and C. Haberland. Control loops with detection of inner electrical resistance and fatigue-behaviour by activation of niti - shape memory alloys. *Proceedings of the 2009 European Symposium on Martensitic Transformations*, 05006:1–8, 2009.

[40] Shu-Hung Liu, Tse-Shih Huang, and Jia-Yush Yen. Tracking control of shape-memory-alloy actuators based on self-sensing feedback and inverse hysteresis compensation. *Sensors*, 10:112–127, 2010.

[41] N. Ma, G. Song, and H.J. Lee. Position control of shape memory alloy actuators with internal electrical resistance feedback using neural networks. *Smart Materials and Structures*, 13:777–783, 2004.

[42] Estibalitz Asua, Jorge Feutchwanger, Alfredo Garcia-Arribas, and Victor Etxebarria. Sensorless control of sma-based actuators using neural networks. *Journal of Intelligent Material Systems and Structures*, 21:1809–1818, 2010.

[43] Junichi Urata, Tomoaki Yoshikai, Ikuo Mizuuchi, and Masayuki Inaba. Design of high d.o.f. mobile micro robot using electrical resistance control of shape memory alloy. *Proceedings of the 2007 IEEE/RSJ International Conference on Intelligent Robots and Systems*, pages 3828–3833, 2007.